



Rydberg exciton–polaritons in a Cu₂O microcavity

Konstantinos Orfanakis^{1,7}, Sai Kiran Rajendran^{1,7}, Valentin Walther^{2,3}, Thomas Volz^{4,5},
Thomas Pohl⁶ and Hamid Ohadi¹✉

Giant Rydberg excitons with principal quantum numbers as high as $n=25$ have been observed in cuprous oxide (Cu₂O), a semiconductor in which the exciton diameter can become as large as $\sim 1\mu\text{m}$. The giant dimension of these excitons results in excitonic interaction enhancements of orders of magnitude. Rydberg exciton–polaritons, formed by the strong coupling of Rydberg excitons to cavity photons, are a promising route to exploit these interactions and achieve a scalable, strongly correlated solid-state platform. However, the strong coupling of these excitons to cavity photons has remained elusive. Here, by embedding a thin Cu₂O crystal into a Fabry–Pérot microcavity, we achieve strong coupling of light to Cu₂O Rydberg excitons up to $n=6$ and demonstrate the formation of Cu₂O Rydberg exciton–polaritons. These results pave the way towards realizing strongly interacting exciton–polaritons and exploring strongly correlated phases of matter using light on a chip.

Exciton–polaritons in semiconductor microcavities^{1–4} have emerged as versatile light–matter interfaces that have led to remarkable developments in fundamental science and technology⁵, from the observation of high-temperature Bose–Einstein condensation^{6–8} and topological states⁹ to future applications for scalable quantum simulations¹⁰ and polaritonic devices¹¹. While experiments have been able to exploit exciton–exciton interactions to demonstrate optical nonlinearities^{12,13} and non-classical effects^{14–17} at high light intensities, the realization of strong and controllable interactions remains an important frontier that would bring applications into the quantum domain. High-lying excitonic Rydberg states offer such interactions, and in particular cuprous oxide (Cu₂O) has been identified as a well-suited material with giant Rydberg excitons as large as $\sim 1\mu\text{m}$ (ref. ¹⁸) resulting in strong blockade effects¹⁹. Yet, harnessing these interactions for applications has remained a challenge due to the weak light–matter coupling in this material.

Highly excited Rydberg excitons are difficult to find due to the small Rydberg constant of most materials. Cu₂O with a large Rydberg constant of $\mathcal{R} = 97\text{ meV}$ is a rare exception, showing Rydberg states with record principal quantum numbers of $n=30$ (refs. ^{18,20}). In such highly excited states, excitons become very sensitive to external fields^{21,22} and feature mutual interactions that can be enhanced by more than ten orders of magnitude over that of the ground state¹⁹. The lowest conduction band and the highest valence band in Cu₂O have the same parity, such that the direct dipole transition in Cu₂O is parity forbidden²³ and leads to a Rydberg series of long-lived P-state excitons. Based on the linewidths observed for Rydberg excitons up to $n=25$ (ref. ¹⁸), lifetimes of 200–400 ps can be anticipated, an order of magnitude larger than excitons in GaAs quantum wells. The associated long coherence times²⁴ combined with the strong Rydberg-state interactions hold great promise for a broad range of applications^{25,26}. The renewed interest in excitons of Cu₂O has led to a large number of studies, as detailed in recent review articles^{27,28}.

The enhanced coherence, however, comes at a cost as the forbidden dipole transition also implies a small oscillator strength and correspondingly weak coupling of light to Rydberg excitons in

Cu₂O. Here we solve this problem by embedding a natural Cu₂O crystal between two highly reflective distributed Bragg reflectors (DBRs) (Fig. ^{1b}). Our fabricated Cu₂O microcavity reaches the strong light–matter coupling regime for Rydberg excitons with up to $n=6$. This, in turn, makes it possible to form Rydberg exciton–polaritons, which we demonstrate using transmission microscopy with high spectral and spatial resolution. The ability to generate exciton–polaritons in high-lying Rydberg states opens the door to exploring quantum many-body phenomena of interacting photons²⁹ and complex quantum states of light³⁰.

Optical resonators can enhance light–matter coupling and hybridize photons and excitons in a semiconductor. This hybridization results in the emergence of polaritons, which behave as quasiparticles that can be observed as distinct resonances in spectroscopic measurements. Strong coupling to excited exciton states generates so-called Rydberg polaritons that inherit the special properties of Rydberg excitons^{18,19} as demonstrated and exploited successfully in atomic systems in recent years^{31,32}. The yellow series of P-state excitons in Cu₂O features a large number of such exciton states that give rise to a series of narrow absorption peaks (Fig. ^{1a}). This Rydberg series overlaps with a broad absorption background that emerges above the energy of the 1S-*ortho* exciton and originates from the virtual population of blue excitons, which subsequently decay into an optical phonon and the 1S-*ortho* exciton³³. It turns out that the interplay of these two absorption channels gives rise to characteristic polariton resonances that we can probe and analyse via cavity-transmission spectroscopy.

Results

Absorption spectrum of Cu₂O. To examine the optical properties of our Cu₂O crystal, we cut a mined Cu₂O crystal along the [111] crystallographic plane, mechanically polish it and thin it to a few tens of micrometres (see Methods and Supplementary Information, section 1 for more details). The surface quality of the crystal after polishing is confirmed by bright- and dark-field microscopy. The sample is placed between two CaF₂ windows and mounted gently on a cold finger in a cryostat, ensuring that the strain on the

¹SUPA, School of Physics and Astronomy, University of St Andrews, St Andrews, UK. ²ITAMP, Harvard-Smithsonian Center for Astrophysics, Cambridge, MA, USA. ³Department of Physics, Harvard University, Cambridge, MA, USA. ⁴School of Mathematical and Physical Sciences, Macquarie University, Sydney, New South Wales, Australia. ⁵ARC Centre of Excellence for Engineered Quantum Systems, Macquarie University, Sydney, New South Wales, Australia. ⁶Center for Complex Quantum Systems, Department of Physics and Astronomy, Aarhus University, Aarhus, Denmark. ⁷These authors contributed equally: Konstantinos Orfanakis, Sai Kiran Rajendran. ✉e-mail: ho35@st-andrews.ac.uk

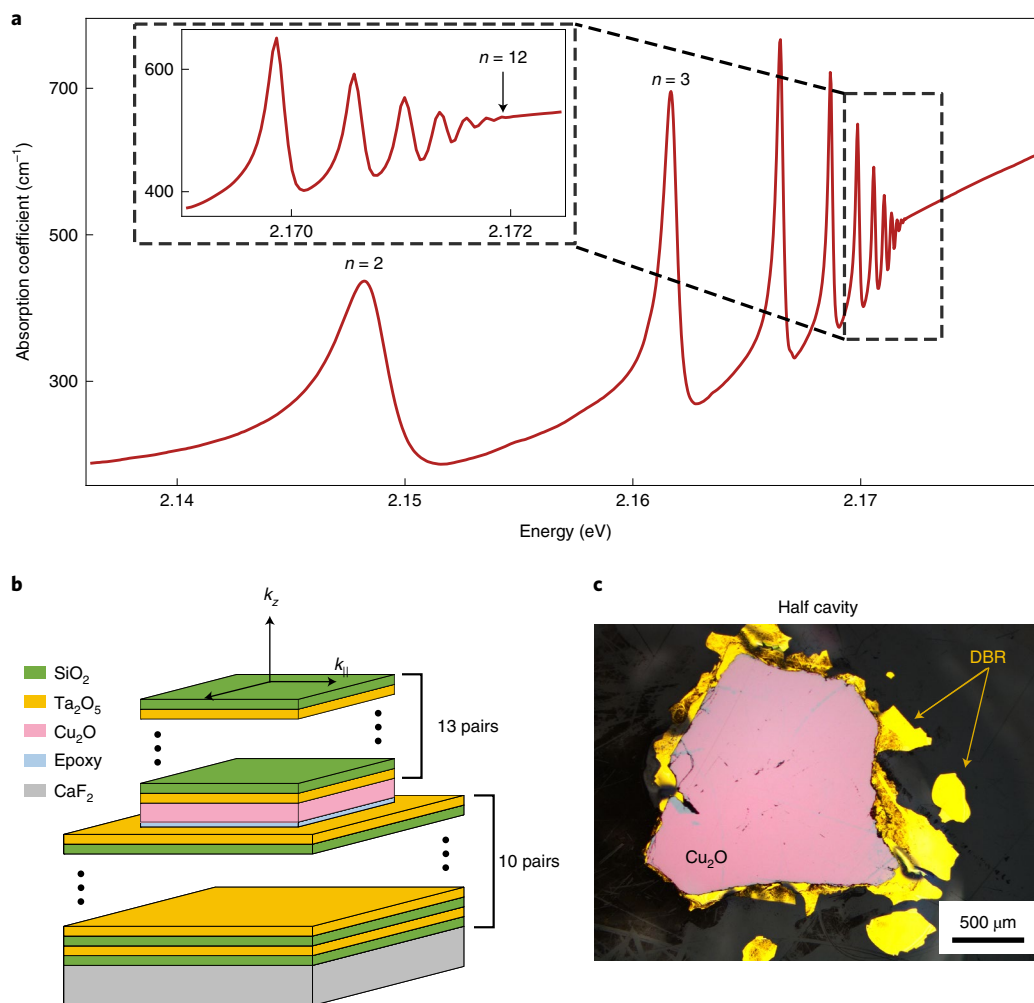


Fig. 1 | Absorption spectrum and cavity structure. **a**, Absorption coefficient α for a natural crystal of Cu_2O at 4 K measured in free space, where excitons up to $n=12$ are resolved. The excitation source is a broadband LED (Supplementary Information, section 2). Inset: higher-energy region of the spectrum. **b**, Schematic illustration of the microcavity with the embedded Cu_2O crystal. **c**, Bright-field optical microscopy image of the half cavity. Note that the Cu_2O sample used in the cavity (**c**) is different from that used for the absorption measurements (**a**).

crystal due to the substrate is minimized as the crystal cools down to cryogenic temperatures. For optical excitation, we use a green–yellow light-emitting diode (LED) with a centre wavelength of 554 nm, and a spectrally filtered supercontinuum white-light laser (Supplementary Information, section 2). The absorption spectrum at $T=4$ K reveals Rydberg states up to $n=12$ and the continuous absorption background discussed above (Fig. 1a). The asymmetric Fano profile of the exciton resonances caused by this background³⁴ is clearly visible. The smaller number of observed exciton lines compared with previous measurements¹⁸ is due to the resolution of our spectrometer, the broadband spectrum of our excitation source, the higher temperature of the crystal ($T=4$ K) and the crystal quality.

Fabry–Pérot microcavity. To achieve strong photon coupling to these excitons, we fabricate a planar Fabry–Pérot microcavity by placing a new crystal between highly reflective mirrors. Two DBRs form the top and bottom mirrors, with 13 and 10 pairs of $\text{SiO}_2/\text{Ta}_2\text{O}_5$ layers (Fig. 1b). We can obtain the quality factor of our cavity by measuring the cavity-transmission linewidth at normal incidence away from any exciton resonance. The experiment yields a quality factor $Q \approx 1,700$ that is smaller than the predicted value $Q \approx 2,300$, which does not include the inhomogeneous broadening due to local cavity thickness modulation caused by DBR deposition, polishing

and the wedged structure of the cavity. From the experimental free spectral range of ~ 6.6 meV, we estimate an active layer thickness of $l \approx 31 \mu\text{m}$. Figure 1c shows a bright-field reflectivity image of this thin layer before depositing the top DBR, confirming the successful integration of the mirror and a smooth, millimetre-sized Cu_2O sample with micrometre-scale thickness.

Exciton–polariton dispersion. We analyse the coupling between the photons and Rydberg excitons by measuring the polaritonic energy dispersion as a function of the in-plane wavevector k_{\parallel} of our microcavity using a Fourier space imaging set-up (Supplementary Information, section 2). The planar microcavity produces longitudinal confinement of the light at the resonant wavelength λ_c and corresponding frequency ω_c . For a single coupled longitudinal mode, the cavity photons thus acquire a quadratic dispersion $E \approx \hbar\omega_c + \hbar^2 k_{\parallel}^2 / 2m_{\text{cav}}$, where \hbar is the reduced Planck constant, akin to particles moving in the transverse plane of the cavity mirrors with an effective mass m_{cav} (ref. 35). Due to the much larger mass of the excitons, the excitonic dispersion is virtually flat for relevant in-plane momenta k_{\parallel} , and may cross the photon mode at the exciton energy. At sufficiently strong light–matter coupling, this gives rise to an avoided crossing and two new modes (upper and lower exciton–polariton) that are separated by the vacuum Rabi splitting

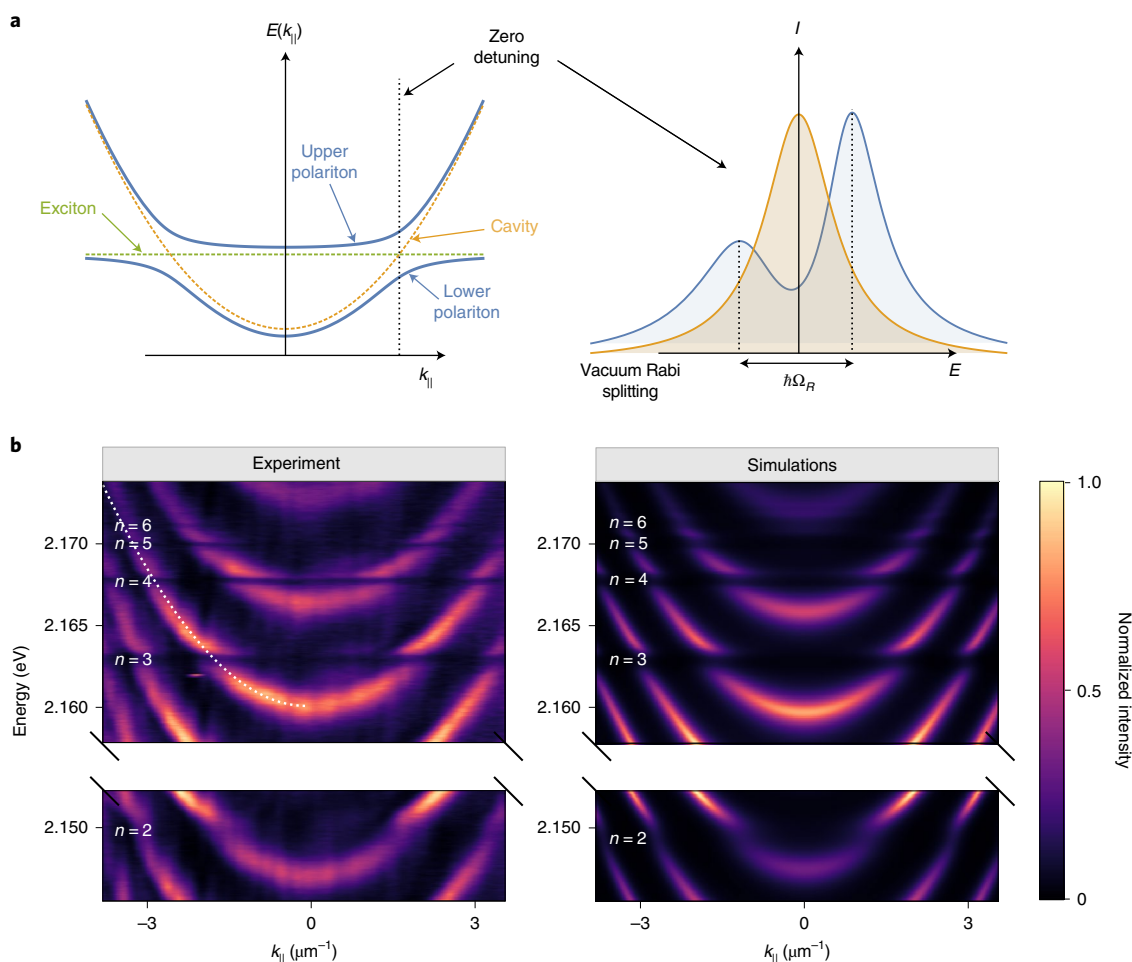


Fig. 2 | Momentum-space spectra. **a**, Left panel: the parabolic cavity dispersion (dotted orange) near an exciton transition (dotted green) modifies to an avoided crossing with two modes (upper and lower polariton, solid blue). Zero detuning (dotted line) is where the cavity and exciton modes cross. Right panel: the energy line profile at zero detuning (cavity resonant with exciton) shows a mode splitting equal to the vacuum Rabi splitting $\hbar\Omega_R$. **b**, Momentum-resolved transmission at 4 K from experiment (left) and transfer matrix method simulations (right). The dotted line shows the cavity mode. The excitation source in **b** is a top-hat resonant pulsed laser (Supplementary Information, section 2).

$\hbar\Omega_R$ (Fig. 2a). Our angle-resolved transmission spectrum reveals this exciton–photon hybridization and demonstrates the formation of exciton–polaritons under strong coupling conditions for Rydberg states with $n = 3, \dots, 6$ (Fig. 2b). While the linewidth of the P-exciton ground state ($n = 2$) is too large to reach the strong coupling regime, the increasingly longer lifetime of the excited states makes it possible to form Rydberg polaritons under the conditions of our experiment in excellent agreement with the theoretical expectation based on transfer matrix calculations.

Asymmetric exciton–polariton dispersion. The large size of the sample makes it possible to scan the photon dispersion through the exciton resonance. To this end, we exploit the slightly wedged structure of the crystal after polishing ($\sim 0.6^\circ$). We vary the excitation position of the incident field to control the relevant thickness of the cavity, thereby tuning the energy of the cavity mode. By using a position scanner with a spatial resolution of 30 nm per step, the cavity transmission spectra can be scanned with high precision ($\sim 13 \mu\text{eV}$ per step), and reveals clear resonances as the cavity energy ($E_{\text{cav}} = \hbar\omega_c$) hits the exciton energies of the Rydberg series (E_n) (Fig. 3). To determine the cavity–exciton detuning, $E_{\text{cav}} - E_n$, the nearest cavity mode needs to be identified for each Rydberg state. The cavity modes outside the yellow exciton transitions can be easily identified as they are far detuned from any excitons. From

this, the cavity modes near the excitons can then be calculated by a simple energy translation since the cavity modes are equally spaced in energy by $hc/(2\bar{n}l)$, where c is the speed of light, h is the Planck constant, l is the cavity thickness and \bar{n} is the real refractive index of Cu_2O (see also Supplementary Information, section 3). A cavity mode comes into resonance with each Rydberg exciton transition as l is scanned, and shows a clear splitting of the polariton modes for $n = 3, \dots, 6$.

Interestingly, the amplitude of the transmission peaks of the upper and lower polaritons is not symmetric. This reflects the asymmetry of the exciton line, which originates from the continuous absorption background^{18,34} discussed above, resulting in a Fano absorption profile $\alpha_n \propto \frac{\bar{\gamma}_n/2 + 2Q_n\Delta_n}{(\bar{\gamma}_n/2)^2 + \Delta_n^2}$ with an asymmetry parameter $Q_n \neq 0$, a transition linewidth $\bar{\gamma}_n$, and a laser detuning $\Delta_n = \omega_{\text{in}} - E_n/\hbar$, where ω_{in} is the angular frequency of the laser. Taking into account the underlying phonon-assisted absorption process, one can derive a simple expression for the resonant cavity transmission spectrum for the case when the cavity and a single exciton transition are resonant (see Methods for more details)

$$T_n \approx \frac{1}{\left(\frac{\bar{\kappa}}{2} + G_n^2 \frac{\bar{\gamma}_n/2 + 2Q_n\Delta_n}{(\bar{\gamma}_n/2)^2 + \Delta_n^2}\right)^2 + \left(\Delta_n - G_n^2 \frac{\Delta_n - Q_n\bar{\gamma}_n}{(\bar{\gamma}_n/2)^2 + \Delta_n^2}\right)^2} \quad (1)$$

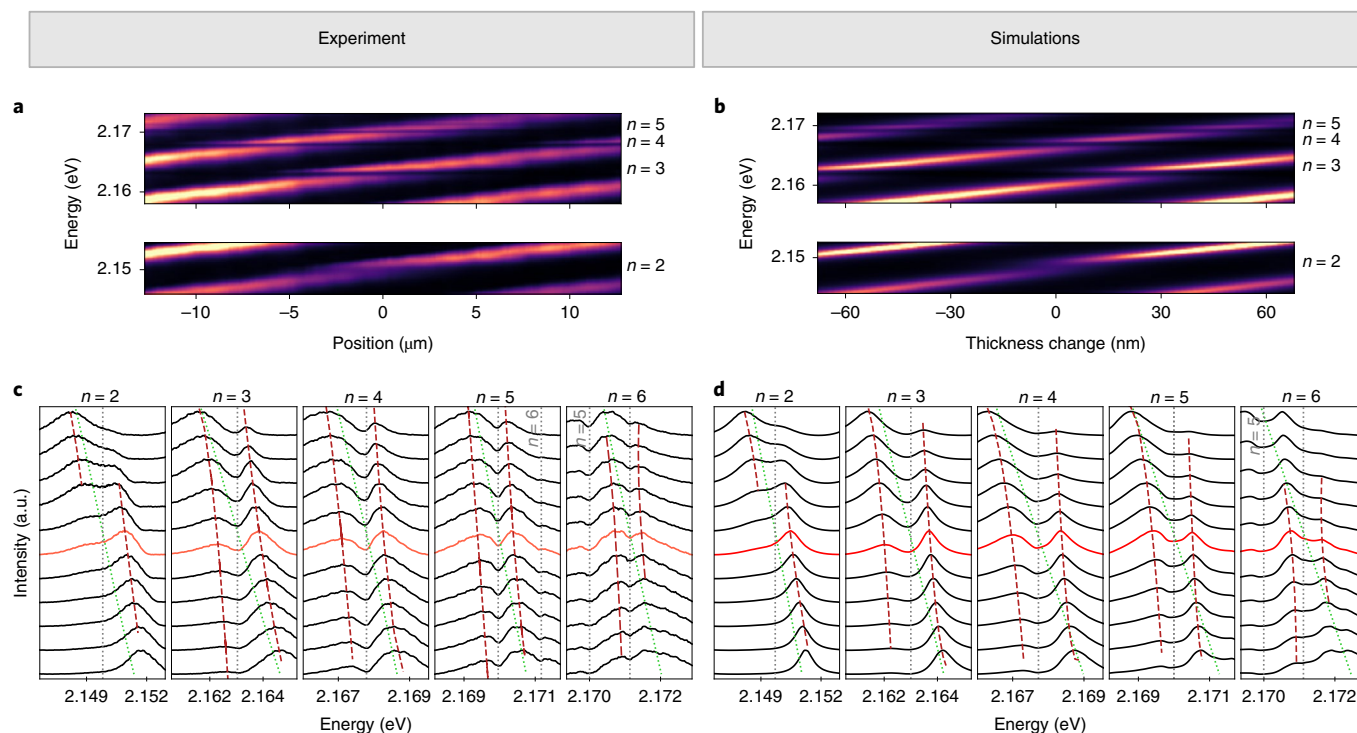


Fig. 3 | Real-space spectra. **a–d**, Experimental (**a**) and simulated (**b**) real-space spectra at $T = 4$ K in the vicinity of the first five P exciton states, and the corresponding intensity line profiles (**c,d**). Dotted lines represent the exciton (grey) and cavity modes (green). Dashed lines trace the upper and lower polariton branches. The orange lined spectrum is the line profile at zero detuning. The excitation source is a top-hat resonant pulsed laser (Supplementary Information, section 2).

which gives transmission maxima at the expected polariton resonances as a function of the laser detuning Δ_n . Here, $\tilde{\kappa}$ is the cavity linewidth far off-resonance, which includes losses from the phonon background. Equation (1) quantitatively explains the asymmetric transmission peaks observed in our experiments (Fig. 4a). By fitting this expression to our measured resonant transmission spectra (Supplementary Information, section 3), we can deduce the exciton–cavity coupling strength G_n . Considering that there is only one fitting parameter G_n and all other parameters in equation (1) are obtained from independent measurements (see Supplementary Table 1 for a full list of parameters), our theory yields remarkably good agreement with the measurements. From the theoretical line profiles, we can obtain the minimum value of G_n required to observe clearly separated polariton resonances (Fig. 4b and Supplementary Information, section 4). The depicted comparison with the measured values of G_n , shows that our cavity just reaches the onset of the strong coupling regime for $n = 2$ and shows Rydberg polaritons well within the strong coupling regime for $n = 3, \dots, 6$.

Exciton–photon coupling strength. The photon coupling G_n decreases with n , reflecting the Rydberg scaling of the oscillator strength¹⁸ (Fig. 5), such that the strong-coupling condition is ultimately limited by the competition with the linewidth of the formed polaritons. The photon coupling can, in principle, be made stronger by increasing the cavity thickness because a larger volume of the active medium collectively enhances the exciton–photon coupling. However, the phonon-induced absorption background in Cu_2O represents another photon-loss mechanism that adds to the linewidth of the cavity. Our transfer matrix calculations indicate that this competition leads to a finite ratio of the vacuum Rabi splitting to the linewidth of the polaritons as one increases the cavity thickness (Supplementary Information, section 5). Without the phonon absorption background, the calculations

yield a steadily increasing ratio of the Rabi splitting to the polariton linewidth with increasing crystal thickness. With the phonon absorption background, the calculations also predict strong coupling for all Rydberg states observed in the bulk crystal, but the coupling strength plateaus as cavity thickness increases (Supplementary Information, section 5). The question then arises as to why in the experiment we are limited to $n = 6$ for strong coupling if we can observe states up to $n = 12$ in the bulk. This could be for a few reasons: the plasma effect, the blockade effect, external strain or charged defects in the crystal. The in-cavity intensity is sufficiently low that the plasma effect³⁶ and the blockade effect can be neglected (Supplementary Information, section 6). Our careful step-by-step spectroscopy during the fabrication process on a different sample shows that despite introducing some strain on our crystal, the effect is not notable enough to at least $n = 9$ (Supplementary Information, section 7). We therefore believe that the quality of this particular crystal in our microcavity was not as high as that shown in Fig. 1.

Discussion

It is pertinent to compare our work to current research on Rydberg exciton–polaritons in other materials. Recent work has achieved strong cavity coupling to excited exciton states in monolayers of WSe_2 (ref. 37) and in a perovskite cavity containing single-crystal CsPbBr_3 microplates³⁸ (see Supplementary Information, section 8 for a more detailed comparison). Whereas all previous observations of exciton–polaritons have been limited to $n = 2$, Cu_2O has the great advantage that narrow exciton lines with up to $n = 12$ can be routinely detected and now makes it possible to realize Rydberg polaritons with $n = 6$ in the presence of phonon coupling. Our calculations show that with experimentally feasible cavity thicknesses, non-classical light can be observed even for $n = 6$ polaritons (Supplementary Information, section 6).

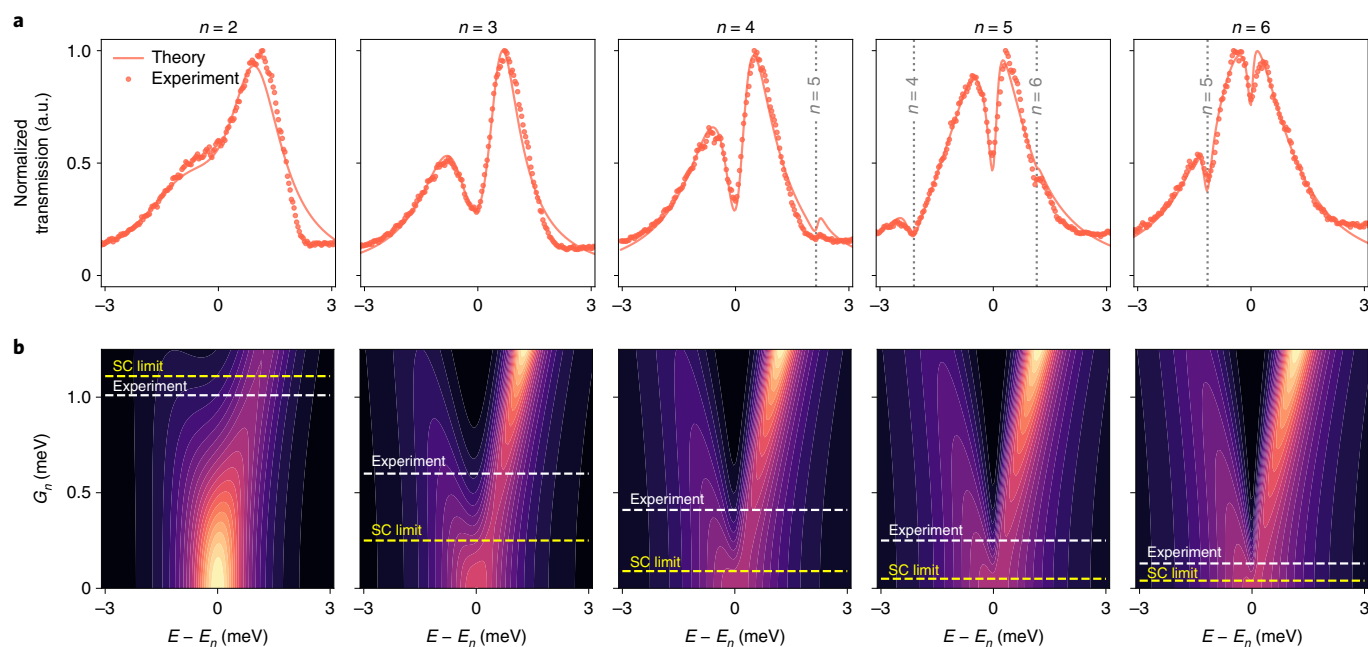


Fig. 4 | Zero-detuning line profiles and the effective coupling strength. **a**, Experimental data and fitted lines for the lower and upper polariton branches at zero detuning (cavity resonant with exciton) for the $n=2, 3, 4, 5$ and 6 exciton states. The excitation source in **a** is a top-hat resonant pulsed laser (Supplementary Information, section 2). The small mismatch between the theory fits and the experiment at positive energies is due to the asymmetric cavity line profile (Supplementary Information, section 3). **b**, Theoretical contour plots of the effective coupling strength, G_n , as a function of detuning for the $n=2, 3, 4, 5$ and 6 exciton states. The strong coupling transition is depicted as a yellow dashed line, while the experimentally obtained coupling strength is shown as a white dashed line.

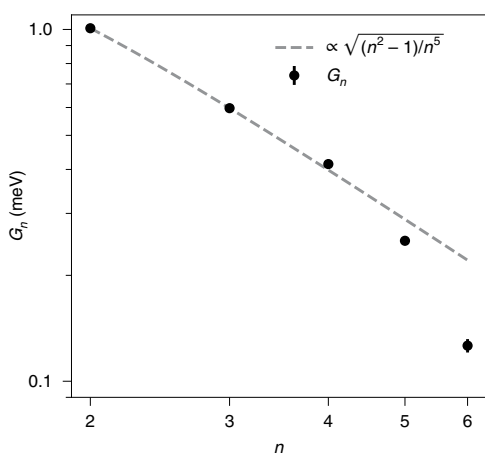


Fig. 5 | Scaling of coupling strength. Effective coupling strength parameter G_n versus quantum number n in the experiment (circles), and the square root of the theoretical oscillator strength (dashed line) show agreement with each other. The error bars (vertical lines) represent fitting errors.

The phonon-induced absorption background can be eliminated via two-photon coupling to Rydberg S-state excitons³⁹, which will thus make it possible to achieve strong cavity coupling with even higher-lying Rydberg states. The demonstrated possibility to generate multiple excited levels in semiconductor microcavities will also permit the realization of electromagnetically induced transparency, whereby a low-lying P exciton can be strongly coupled to cavity photons and the transition to a highly excited S-state exciton is driven by an external control field^{39,40}. These Rydberg electromagnetically induced transparency settings, which exploit the strong van der Waals interaction between high-lying Cu_2O Rydberg excitons⁴¹, suggest exciting

possibilities when combined with semiconductor microcavities. The results of our work thus present an essential step towards such new explorations of Rydberg polaritons in the quantum regime.

With their greatly enhanced nonlinearities¹⁹, induced by strong and long-range exciton interactions, Cu_2O Rydberg exciton–polaritons provide a versatile platform for exploring quantum many-body phenomena, extending the physics of weakly interacting photon fluids achievable with low-lying exciton states^{5,16,42}. Previous measurements¹⁸ suggest a blockade diameter of $\sim 0.5\ \mu\text{m}$ for $n=6$, and can reach values of $\sim 2\ \mu\text{m}$ for $n=10$. The associated polariton blockade under strong cavity coupling thus offers a promising approach for generating and manipulating non-classical states of light⁴³, whereby the use of synthetic Cu_2O microcrystals^{44–48} and microscale patterning^{49,50} would yield configurable lattices of strongly interacting individual polaritons.

Online content

Any methods, additional references, Nature Research reporting summaries, source data, extended data, supplementary information, acknowledgements, peer review information; details of author contributions and competing interests; and statements of data and code availability are available at <https://doi.org/10.1038/s41563-022-01230-4>.

Received: 23 August 2021; Accepted: 4 March 2022;

Published online: 14 April 2022

References

- Weisbuch, C., Nishioka, M., Ishikawa, A. & Arakawa, Y. Observation of the coupled exciton–photon mode splitting in a semiconductor quantum microcavity. *Phys. Rev. Lett.* **69**, 3314–3317 (1992).
- Lidzey, D. G. et al. Strong exciton–photon coupling in an organic semiconductor microcavity. *Nature* **395**, 53–55 (1998).
- Dufferwiel, S. et al. Exciton–polaritons in van der Waals heterostructures embedded in tunable microcavities. *Nat. Commun.* **6**, 8579 (2015).

4. Fieramosca, A. et al. Two-dimensional hybrid perovskites sustaining strong polariton interactions at room temperature. *Sci. Adv.* **5**, eaav9967 (2019).
5. Carusotto, I. & Ciuti, C. Quantum fluids of light. *Rev. Mod. Phys.* **85**, 299–366 (2013).
6. Kasprzak, J. et al. Bose–Einstein condensation of exciton polaritons. *Nature* **443**, 409 (2006).
7. Plumhof, J. D., Stöferle, T., Mai, L., Scherf, U. & Mahr, R. F. Room-temperature Bose–Einstein condensation of cavity exciton–polaritons in a polymer. *Nat. Mater.* **13**, 247–252 (2014).
8. Su, R. et al. Observation of exciton polariton condensation in a perovskite lattice at room temperature. *Nat. Phys.* **16**, 301–306 (2020).
9. Klembt, S. et al. Exciton–polariton topological insulator. *Nature* **562**, 552–556 (2018).
10. Amo, A. & Bloch, J. Exciton–polaritons in lattices: a non-linear photonic simulator. *C. R. Phys.* **17**, 934–945 (2016).
11. Sanvitto, D. & Kéna-Cohen, S. The road towards polaritonic devices. *Nat. Mater.* **15**, 1061 (2016).
12. Ballarini, D. et al. All-optical polariton transistor. *Nat. Commun.* **4**, 1778 (2013).
13. Zasedatelev, A. V. et al. A room-temperature organic polariton transistor. *Nat. Photonics* **13**, 378–383 (2019).
14. Boulier, T. et al. Polariton-generated intensity squeezing in semiconductor micropillars. *Nat. Commun.* **5**, 3260 (2014).
15. Cuevas, A. et al. First observation of the quantized exciton–polariton field and effect of interactions on a single polariton. *Sci. Adv.* <https://www.science.org/doi/10.1126/sciadv.aao6814> (2018).
16. Muñoz-Matutano, G. et al. Emergence of quantum correlations from interacting fibre-cavity polaritons. *Nat. Mater.* **18**, 213–218 (2019).
17. Delteil, A. et al. Towards polariton blockade of confined exciton–polaritons. *Nat. Mater.* **18**, 219–222 (2019).
18. Kazimierzczuk, T., Fröhlich, D., Scheel, S., Stolz, H. & Bayer, M. Giant Rydberg excitons in the copper oxide Cu_2O . *Nature* **514**, 343–347 (2014).
19. Heckötter, J. et al. Asymmetric Rydberg blockade of giant excitons in cuprous oxide. *Nat. Commun.* **12**, 3556 (2021).
20. Versteegh, M. A. M. et al. Giant Rydberg excitons in Cu_2O probed by photoluminescence excitation spectroscopy. *Phys. Rev. B* **104**, 245206 (2021).
21. Thewes, J. et al. Observation of high angular momentum excitons in cuprous oxide. *Phys. Rev. Lett.* **115**, 027402 (2015).
22. Heckötter, J. et al. High-resolution study of the yellow excitons in Cu_2O subject to an electric field. *Phys. Rev. B* **95**, 035210 (2017).
23. Schweiner, F., Main, J., Feldmaier, M., Wunner, G. & Uihlein, C. Impact of the valence band structure of Cu_2O on excitonic spectra. *Phys. Rev. B* **93**, 195203 (2016).
24. Kitamura, T., Takahata, M. & Naka, N. Quantum number dependence of the photoluminescence broadening of excitonic Rydberg states in cuprous oxide. *J. Lumin.* **192**, 808–813 (2017).
25. Saffman, M., Walker, T. G. & Mølmer, K. Quantum information with Rydberg atoms. *Rev. Mod. Phys.* **82**, 2313–2363 (2010).
26. Weimer, H., Müller, M., Lesanovsky, I., Zoller, P. & Büchler, H. P. A Rydberg quantum simulator. *Nat. Phys.* **6**, 382–388 (2010).
27. Semina, M. A. Fine structure of Rydberg excitons in cuprous oxide. *Phys. Solid State* **60**, 1527–1536 (2018).
28. Aßmann, M. & Bayer, M. Semiconductor Rydberg physics. *Adv. Quantum Technol.* **3**, 1900134 (2020).
29. Hartmann, M. J. Quantum simulation with interacting photons. *J. Opt.* **18**, 104005 (2016).
30. Chang, D. E., Vuletić, V. & Lukin, M. D. Quantum nonlinear optics—photon by photon. *Nat. Photonics* **8**, 685–694 (2014).
31. Saffman, M., Walker, T. G. & Mølmer, K. Quantum information with Rydberg atoms. *Rev. Mod. Phys.* **82**, 2313–2363 (2010).
32. Browaeys, A. & Lahaye, T. Many-body physics with individually controlled Rydberg atoms. *Nat. Phys.* **16**, 132–142 (2020).
33. Schöne, F., Stolz, H. & Naka, N. Phonon-assisted absorption of excitons in Cu_2O . *Phys. Rev. B* **96**, 115207 (2017).
34. Toyozawa, Y. Interband effect of lattice vibrations in the exciton absorption spectra. *J. Phys. Chem. Solids* **25**, 59–71 (1964).
35. Kavokin, A. V., Baumberg, J. J., Malpuech, G. & Laussy, F. P. *Microcavities* (Oxford Univ. Press, 2017).
36. Heckötter, J. et al. Rydberg excitons in the presence of an ultralow-density electron–hole plasma. *Phys. Rev. Lett.* **121**, 097401 (2018).
37. Gu, J. et al. Enhanced nonlinear interaction of polaritons via excitonic Rydberg states in monolayer WSe_2 . *Nat. Commun.* **12**, 2269 (2021).
38. Bao, W. et al. Observation of Rydberg exciton polaritons and their condensate in a perovskite cavity. *Proc. Natl Acad. Sci. USA* **116**, 20274–20279 (2019).
39. Walther, V., Grünwald, P. & Pohl, T. Controlling exciton–phonon interactions via electromagnetically induced transparency. *Phys. Rev. Lett.* **125**, 173601 (2020).
40. Walther, V., Johne, R. & Pohl, T. Giant optical nonlinearities from Rydberg excitons in semiconductor microcavities. *Nat. Commun.* **9**, 1309 (2018).
41. Walther, V., Krüger, S. O., Scheel, S. & Pohl, T. Interactions between Rydberg excitons in Cu_2O . *Phys. Rev. B* **98**, 165201 (2018).
42. Delteil, A. et al. Towards polariton blockade of confined exciton–polaritons. *Nat. Mater.* **18**, 219–222 (2019).
43. Gorshkov, A. V., Otterbach, J., Fleischhauer, M., Pohl, T. & Lukin, M. D. Photon–photon interactions via Rydberg blockade. *Phys. Rev. Lett.* **107**, 133602 (2011).
44. Lynch, S. A. et al. Rydberg excitons in synthetic cuprous oxide Cu_2O . *Phys. Rev. Mater.* **5**, 084602 (2021).
45. Steinhauer, S. et al. Rydberg excitons in Cu_2O microcrystals grown on a silicon platform. *Commun. Mater.* **1**, 1–7 (2020).
46. Konzelmann, A., Frank, B. & Giessen, H. Quantum confined Rydberg excitons in reduced dimensions. *J. Phys. B* **53**, 024001 (2019).
47. Ziemkiewicz, D., Karpiński, K., Czajkowski, G. & Zielińska-Raczyńska, S. Excitons in Cu_2O : from quantum dots to bulk crystals and additional boundary conditions for Rydberg exciton–polaritons. *Phys. Rev. B* **101**, 205202 (2020).
48. Orfanakis, K. et al. Quantum confined Rydberg excitons in Cu_2O nanoparticles. *Phys. Rev. B* **103**, 245426 (2021).
49. Jacqmin, T. et al. Direct observation of Dirac cones and a flatband in a honeycomb lattice for polaritons. *Phys. Rev. Lett.* **112**, 116402 (2014).
50. Ohadi, H. et al. Synchronization crossover of polariton condensates in weakly disordered lattices. *Phys. Rev. B* **97**, 195109 (2018).

Publisher's note Springer Nature remains neutral with regard to jurisdictional claims in published maps and institutional affiliations.

© The Author(s), under exclusive licence to Springer Nature Limited 2022

Methods

Sample. Polishing and thinning. We start by cleaving a piece from a bulk natural Cu_2O crystal obtained from the Tsumeb mine in Namibia. It is essential that at least one surface of this piece is aligned with one of the crystallographic axes of the crystal, which is evidenced by a highly reflective, metallic-like, smooth surface. A fibre ferrule is then coated with an ethanol-soluble fast-acting adhesive. The sample is mounted on the ferrule with its natural facet side on top of the ferrule. This practice ensures that the sample will be aligned with one crystallographic axis after thinning. For thinning and polishing, we use lapping sheets of different grits (from 16 μm down to 0.3 μm) commonly used for polishing fibres. The ferrule is mounted on a polishing puck which ensures that it is held perpendicular to the polishing paper. By moving the puck over the grit in a figure of eight, excess material from the crystal surface is removed. Every sample undergoes multiple polishing cycles, with inspection under a commercial microscope to ensure there are no features greater than the polishing grit. Once the polishing procedure is complete, we dissolve the glue with ethanol to separate the ferrule from the Cu_2O crystal. The sample is then placed on top of a DBR-coated CaF_2 window with ultraviolet-cured epoxy. After thinning the crystal down to $\sim 30 \mu\text{m}$ and polishing the second surface, the top DBR is deposited to form a cavity.

DBR coating. The bottom DBR consisting of 10 pairs of alternating 67.6-nm-thick SiO_2 and 98.9-nm-thick Ta_2O_5 layers was sputter deposited at room temperature on CaF_2 substrates to obtain maximum reflectivity at $\sim 575 \text{ nm}$. The Cu_2O crystal was glued to the bottom DBR and a top DBR of 13 pairs of Ta_2O_5 and SiO_2 layers was then deposited directly on the Cu_2O crystal (Supplementary Information, section 1).

Transfer matrix simulations. Using the experimental transmission spectra of Cu_2O at 4 K, the absorption coefficient α (cm^{-1}) of exciton transitions in Cu_2O was measured. The imaginary part of the refractive index (k) was obtained from the relation $\alpha(\lambda) = 4\pi k(\lambda)/\lambda$. The real part of the refractive index (n) was obtained from the Hilbert transform of k . The complex refractive index was then used in the transfer matrix method to obtain the transmission of light through the multilayer DBR microcavity.

Theory. The absorption lines of the yellow series in Cu_2O have an asymmetric curved shape due to interference with a spectrally broad, phonon-assisted background³³. This affects the shape of the transmission resonances in a cavity, as shown below. In the excitation process, an incident photon can either excite any of the Rydberg exciton resonances n , described by \hat{X}_n , or a phonon-assisted continuum of states, described by \hat{Y} , both at centre-of-mass momentum \mathbf{k} . The phonon-assisted states also have an internal (relative) momentum \mathbf{k}' . The coupling of the Rydberg excitons to the phonon background provides an interfering excitation pathway, thus creating a Fano resonance⁵¹,

$$\partial_t \hat{X}_n(\mathbf{k}) = -\frac{\Gamma_n}{2} \hat{X}_n(\mathbf{k}) - ig_n \mathcal{E}(\mathbf{k}) - i \sum_{\mathbf{k}'} h_{n,\mathbf{k},\mathbf{k}'} \hat{Y}(\mathbf{k}, \mathbf{k}') \quad (2)$$

$$\partial_t \hat{Y}(\mathbf{k}, \mathbf{k}') = -\frac{\Gamma_{\mathbf{k},\mathbf{k}'}}{2} \hat{Y}(\mathbf{k}, \mathbf{k}') - ig_{\mathbf{k},\mathbf{k}'}^{\text{bg}} \mathcal{E}(\mathbf{k}) - i \sum_n h_{n,\mathbf{k},\mathbf{k}'} \hat{X}_n(\mathbf{k}), \quad (3)$$

where $g_{\mathbf{k},\mathbf{k}'}^{\text{bg}}$ denotes the optical coupling rate to the phononic (background) states, $h_{n,\mathbf{k},\mathbf{k}'}$ the exciton–phonon coupling and $\Gamma_{\mathbf{k},\mathbf{k}'} = \gamma_{\mathbf{k},\mathbf{k}'} - 2i\Delta_{\mathbf{k},\mathbf{k}'}$ the complex phonon linewidth with linewidth $\gamma_{\mathbf{k},\mathbf{k}'}$ and detuning $\Delta_{\mathbf{k},\mathbf{k}'} = \omega_{\text{in}} - \omega_{\mathbf{k},\mathbf{k}'}$, and Γ_n is equivalently defined for the n th exciton. The variables associated with the Rydberg resonance are defined equivalently. The field \mathcal{E} can be understood to give rise to a photon density $\langle \mathcal{E}^\dagger(\mathbf{k}) \mathcal{E}(\mathbf{k}) \rangle$ in mode \mathbf{k} . In the above description, we neglect small contributions from scattering processes involving multiple different phonons. In the steady state, we can solve for the continuum operators

$$\langle \hat{Y}(\mathbf{k}, \mathbf{k}') \rangle = \frac{2}{\Gamma_{\mathbf{k},\mathbf{k}'}} \left[-ig_{\mathbf{k},\mathbf{k}'}^{\text{bg}} \mathcal{E}(\mathbf{k}) - i \sum_n h_{n,\mathbf{k},\mathbf{k}'} \langle \hat{X}_n(\mathbf{k}) \rangle \right]. \quad (4)$$

The phonon states can be assumed as flat ($g_{\mathbf{k},\mathbf{k}'}^{\text{bg}} = g_{\mathbf{k}}^{\text{bg}}$ and $h_{n,\mathbf{k},\mathbf{k}'} = h_{n,\mathbf{k}}$) and dense in the relative momentum quantum number, allowing the sums to be evaluated

$$\begin{aligned} \sum_{\mathbf{k}'} h_{n,\mathbf{k},\mathbf{k}'} \langle \hat{Y}(\mathbf{k}, \mathbf{k}') \rangle &\approx \left[-ih_{n,\mathbf{k}} g_{\mathbf{k}}^{\text{bg}} \mathcal{E}(\mathbf{k}) - ih_{n,\mathbf{k}}^2 \langle \hat{X}_n(\mathbf{k}) \rangle \right] \tau_{k,n} \\ &= -i\bar{h}_{n,\mathbf{k}} g_{n,\mathbf{k}}^{\text{bg}} \mathcal{E}(\mathbf{k}) - i\bar{h}_{n,\mathbf{k}}^2 \langle \hat{X}_n(\mathbf{k}) \rangle, \end{aligned} \quad (5)$$

where we defined $\tau_{k,n} \equiv \tau_k(\omega_{\text{in}} = \omega_n)$ from $\tau_k(\omega_{\text{in}}) = \sum_{\mathbf{k}'} \frac{2}{\Gamma_{\mathbf{k},\mathbf{k}'}}$ and absorbed it into $\bar{h}_{n,\mathbf{k}} \equiv \sqrt{\tau_{k,n}} h_{n,\mathbf{k}}$ and, similarly, $g_{n,\mathbf{k}}^{\text{bg}}$ (which have units $\sim \sqrt{\text{energy}}$). We also neglected small contributions from off-resonant Rydberg states. While $\bar{h}_{n,\mathbf{k}}$ and $g_{n,\mathbf{k}}^{\text{bg}}$ can, in general, carry complex signatures of the underlying decay rates, we assume

them here as real and constant across each exciton resonance. The polarization, $\mathcal{P}(\mathbf{k}) = \chi_{\mathbf{k}} \mathcal{E}(\mathbf{k})$, can be solved explicitly, and defines $\chi_{\mathbf{k}}$ via

$$\begin{aligned} \mathcal{P}(\mathbf{k}) &= \sum_n g_n \langle \hat{X}_n(\mathbf{k}) \rangle + \sum_{\mathbf{k}'} g_{\mathbf{k},\mathbf{k}'}^{\text{bg}} \langle \hat{Y}(\mathbf{k}, \mathbf{k}') \rangle \\ &= -i \sum_n \frac{(g_n - ig_{n,\mathbf{k}}^{\text{bg}} \bar{h}_{n,\mathbf{k}})^2}{\Gamma_n + \bar{h}_{n,\mathbf{k}}^2} \mathcal{E}(\mathbf{k}) - i(g_{\mathbf{k}}^{\text{bg}}(\omega_{\text{in}}))^2 \mathcal{E}(\mathbf{k}) \\ &= -i \sum_n g_n^2 \frac{(1 - iQ_{n,\mathbf{k}})^2}{\Gamma_n - i\Delta_n} \mathcal{E}(\mathbf{k}) - i(g_{\mathbf{k}}^{\text{bg}}(\omega_{\text{in}}))^2 \mathcal{E}(\mathbf{k}), \end{aligned} \quad (6)$$

where we introduced $\bar{\gamma}_n/2 = \gamma_n/2 + \bar{h}_n^2$ and the asymmetry parameter $Q_{n,\mathbf{k}} = \frac{g_{n,\mathbf{k}}^{\text{bg}} \bar{h}_{n,\mathbf{k}}}{g_n}$. The free-space absorption is

$$\alpha_{\mathbf{k}} = -\frac{2}{c\bar{n}} \Im(\chi_{\mathbf{k}}) = \sum_n \frac{4g_n^2 \bar{\gamma}_n + 4Q_{n,\mathbf{k}} \Delta_n}{c\bar{n} \bar{\gamma}_n^2 + 4\Delta_n^2} + \alpha_{\mathbf{k}}^{\text{bg}}(\omega_{\text{in}}) \quad (7)$$

with the refractive index \bar{n} and where we dropped terms $\sim Q_{n,\mathbf{k}}^2$ under the assumption that $Q_{n,\mathbf{k}}^2 \ll 1$. We recognize a constant absorption term from the background, and the plain exciton absorption if $Q_{n,\mathbf{k}} = 0$. The cross-term originates from the interference between direct and indirect excitation of the background and produces an asymmetric lineshape. The standard in-cavity field equation for transverse momentum \mathbf{k}_{\parallel} (ref. 3) is modified into

$$\partial_t \tilde{\mathcal{E}}(\mathbf{k}_{\parallel}) = -\frac{\Gamma_{\text{cav}}}{2} \tilde{\mathcal{E}}(\mathbf{k}_{\parallel}) - \frac{i}{\bar{n}^2} \mathcal{P}(\mathbf{k}_{\parallel}) + \eta_{\text{in}} E^{\text{in}}(\mathbf{k}_{\parallel}) \quad (8)$$

where $\Gamma_{\text{cav}} = \kappa - 2i(\omega_{\text{in}} - (\omega_{\text{cav}} + \hbar k_{\parallel}^2/(2m_{\text{ph}})))$, κ is the cavity linewidth, m_{ph} is the effective transverse photon mass and E^{in} is the external driving field with corresponding coupling η . Transmission through the cavity at fixed \mathbf{k}_{\parallel} is proportional to the in-cavity intensity, $T = C_{\text{out}} |\mathcal{E}|^2$, and is given by

$$\begin{aligned} T &= \left[\left(\frac{\kappa}{2} + \sum_n \left(\frac{g_n}{\bar{n}} \right)^2 \frac{[1 - Q_{n,\mathbf{k}}^2] \bar{\gamma}_n + 2\Delta_n Q_n}{(\bar{\gamma}_n/2)^2 + \Delta_n^2} + \left(\frac{g_{\text{bg}}(\omega_{\text{in}})}{\bar{n}} \right)^2 \right)^2 \right. \\ &\quad \left. + \left(\Delta_{\text{cav}} - \sum_n \left(\frac{g_n}{\bar{n}} \right)^2 \frac{[1 - Q_{n,\mathbf{k}}^2] \Delta_n - Q_n \bar{\gamma}_n}{(\bar{\gamma}_n/2)^2 + \Delta_n^2} \right)^2 \right]^{-1}. \end{aligned} \quad (9)$$

We note that for comparison with equation (7), terms $\sim Q_n^2$ should be dropped, and $G_n = g_n/\bar{n}$ is the effective coupling strength.

Reporting summary. Further information on research design is available in the Nature Research Reporting Summary linked to this article.

Data availability

The research data underpinning this publication can be accessed from University of St Andrews Research Data repository at <https://doi.org/10.17630/4f4e4d92-8309-45db-bade-26b147696138>.

References

- Fano, U. Effects of configuration interaction on intensities and phase shifts. *Phys. Rev.* **124**, 1866–1878 (1961).

Acknowledgements

This work was supported by the EPSRC through grant number EP/S014403/1, by the Royal Society through RGS/R2/192174, by the Carlsberg Foundation through the ‘Semper Ardens’ Research Project QCool, by the NSF through a grant for ITAMP at Harvard University, by the DFG through SPP1929, and by the Danish National Research Foundation through the Center of Excellence ‘CCQ’ (grant agreement number DNR156). K.O. acknowledges the EPSRC for PhD studentship support through grant number EP/L015110/1. S.K.R. acknowledges the Carnegie Trust for the Universities of Scotland Research Incentive Grant RIG009823. T.V. acknowledges support through the Australian Research Council Centre of Excellence for Engineered Quantum Systems (CE170100009). V.W. acknowledges support by the NSF through a grant for the Institute for Theoretical Atomic, Molecular, and Optical Physics at Harvard University and the Smithsonian Astrophysical Observatory. We thank J. Keeling for fruitful discussions. We also thank Y. Nanao and EPSRC grant number EP/T023449/1 for the X-ray diffraction measurements.

Author contributions

K.O. polished the sample, performed spectroscopy and analysed the data. S.K.R. deposited DBRs and performed the transfer matrix simulations. V.W. and T.P. developed the theory. T.V. and H.O. supervised the project. H.O. conceived and designed the project. All authors contributed to the writing of the manuscript.

Competing interests

The authors declare no competing interests.

Additional information

Supplementary information The online version contains supplementary material available at <https://doi.org/10.1038/s41563-022-01230-4>.

Correspondence and requests for materials should be addressed to Hamid Ohadi.

Peer review information *Nature Materials* thanks Na Young Kim and the other, anonymous, reviewer(s) for their contribution to the peer review of this work.

Reprints and permissions information is available at www.nature.com/reprints.

Reporting Summary

Nature Portfolio wishes to improve the reproducibility of the work that we publish. This form provides structure for consistency and transparency in reporting. For further information on Nature Portfolio policies, see our [Editorial Policies](#) and the [Editorial Policy Checklist](#).

Statistics

For all statistical analyses, confirm that the following items are present in the figure legend, table legend, main text, or Methods section.

- | n/a | Confirmed |
|-------------------------------------|---|
| <input checked="" type="checkbox"/> | <input type="checkbox"/> The exact sample size (n) for each experimental group/condition, given as a discrete number and unit of measurement |
| <input type="checkbox"/> | <input checked="" type="checkbox"/> A statement on whether measurements were taken from distinct samples or whether the same sample was measured repeatedly |
| <input checked="" type="checkbox"/> | <input type="checkbox"/> The statistical test(s) used AND whether they are one- or two-sided
<i>Only common tests should be described solely by name; describe more complex techniques in the Methods section.</i> |
| <input checked="" type="checkbox"/> | <input type="checkbox"/> A description of all covariates tested |
| <input checked="" type="checkbox"/> | <input type="checkbox"/> A description of any assumptions or corrections, such as tests of normality and adjustment for multiple comparisons |
| <input checked="" type="checkbox"/> | <input type="checkbox"/> A full description of the statistical parameters including central tendency (e.g. means) or other basic estimates (e.g. regression coefficient) AND variation (e.g. standard deviation) or associated estimates of uncertainty (e.g. confidence intervals) |
| <input checked="" type="checkbox"/> | <input type="checkbox"/> For null hypothesis testing, the test statistic (e.g. F , t , r) with confidence intervals, effect sizes, degrees of freedom and P value noted
<i>Give P values as exact values whenever suitable.</i> |
| <input checked="" type="checkbox"/> | <input type="checkbox"/> For Bayesian analysis, information on the choice of priors and Markov chain Monte Carlo settings |
| <input checked="" type="checkbox"/> | <input type="checkbox"/> For hierarchical and complex designs, identification of the appropriate level for tests and full reporting of outcomes |
| <input checked="" type="checkbox"/> | <input type="checkbox"/> Estimates of effect sizes (e.g. Cohen's d , Pearson's r), indicating how they were calculated |

Our web collection on [statistics for biologists](#) contains articles on many of the points above.

Software and code

Policy information about [availability of computer code](#)

Data collection

Data analysis

For manuscripts utilizing custom algorithms or software that are central to the research but not yet described in published literature, software must be made available to editors and reviewers. We strongly encourage code deposition in a community repository (e.g. GitHub). See the Nature Portfolio [guidelines for submitting code & software](#) for further information.

Data

Policy information about [availability of data](#)

All manuscripts must include a [data availability statement](#). This statement should provide the following information, where applicable:

- Accession codes, unique identifiers, or web links for publicly available datasets
- A description of any restrictions on data availability
- For clinical datasets or third party data, please ensure that the statement adheres to our [policy](#)

The research data underpinning this publication can be accessed at <https://doi.org/10.17630/4f4e4d92-8309-45db-bade-26b147696138>

Field-specific reporting

Please select the one below that is the best fit for your research. If you are not sure, read the appropriate sections before making your selection.

Life sciences Behavioural & social sciences Ecological, evolutionary & environmental sciences

For a reference copy of the document with all sections, see nature.com/documents/nr-reporting-summary-flat.pdf

Life sciences study design

All studies must disclose on these points even when the disclosure is negative.

Sample size	<i>Describe how sample size was determined, detailing any statistical methods used to predetermine sample size OR if no sample-size calculation was performed, describe how sample sizes were chosen and provide a rationale for why these sample sizes are sufficient.</i>
Data exclusions	<i>Describe any data exclusions. If no data were excluded from the analyses, state so OR if data were excluded, describe the exclusions and the rationale behind them, indicating whether exclusion criteria were pre-established.</i>
Replication	<i>Describe the measures taken to verify the reproducibility of the experimental findings. If all attempts at replication were successful, confirm this OR if there are any findings that were not replicated or cannot be reproduced, note this and describe why.</i>
Randomization	<i>Describe how samples/organisms/participants were allocated into experimental groups. If allocation was not random, describe how covariates were controlled OR if this is not relevant to your study, explain why.</i>
Blinding	<i>Describe whether the investigators were blinded to group allocation during data collection and/or analysis. If blinding was not possible, describe why OR explain why blinding was not relevant to your study.</i>

Behavioural & social sciences study design

All studies must disclose on these points even when the disclosure is negative.

Study description	<i>Briefly describe the study type including whether data are quantitative, qualitative, or mixed-methods (e.g. qualitative cross-sectional, quantitative experimental, mixed-methods case study).</i>
Research sample	<i>State the research sample (e.g. Harvard university undergraduates, villagers in rural India) and provide relevant demographic information (e.g. age, sex) and indicate whether the sample is representative. Provide a rationale for the study sample chosen. For studies involving existing datasets, please describe the dataset and source.</i>
Sampling strategy	<i>Describe the sampling procedure (e.g. random, snowball, stratified, convenience). Describe the statistical methods that were used to predetermine sample size OR if no sample-size calculation was performed, describe how sample sizes were chosen and provide a rationale for why these sample sizes are sufficient. For qualitative data, please indicate whether data saturation was considered, and what criteria were used to decide that no further sampling was needed.</i>
Data collection	<i>Provide details about the data collection procedure, including the instruments or devices used to record the data (e.g. pen and paper, computer, eye tracker, video or audio equipment) whether anyone was present besides the participant(s) and the researcher, and whether the researcher was blind to experimental condition and/or the study hypothesis during data collection.</i>
Timing	<i>Indicate the start and stop dates of data collection. If there is a gap between collection periods, state the dates for each sample cohort.</i>
Data exclusions	<i>If no data were excluded from the analyses, state so OR if data were excluded, provide the exact number of exclusions and the rationale behind them, indicating whether exclusion criteria were pre-established.</i>
Non-participation	<i>State how many participants dropped out/declined participation and the reason(s) given OR provide response rate OR state that no participants dropped out/declined participation.</i>
Randomization	<i>If participants were not allocated into experimental groups, state so OR describe how participants were allocated to groups, and if allocation was not random, describe how covariates were controlled.</i>

Ecological, evolutionary & environmental sciences study design

All studies must disclose on these points even when the disclosure is negative.

Study description	<i>Briefly describe the study. For quantitative data include treatment factors and interactions, design structure (e.g. factorial, nested, hierarchical), nature and number of experimental units and replicates.</i>
Research sample	<i>Describe the research sample (e.g. a group of tagged <i>Passer domesticus</i>, all <i>Stenocereus thurberi</i> within Organ Pipe Cactus National</i>

Research sample *Monument), and provide a rationale for the sample choice. When relevant, describe the organism taxa, source, sex, age range and any manipulations. State what population the sample is meant to represent when applicable. For studies involving existing datasets, describe the data and its source.*

Sampling strategy *Note the sampling procedure. Describe the statistical methods that were used to predetermine sample size OR if no sample-size calculation was performed, describe how sample sizes were chosen and provide a rationale for why these sample sizes are sufficient.*

Data collection *Describe the data collection procedure, including who recorded the data and how.*

Timing and spatial scale *Indicate the start and stop dates of data collection, noting the frequency and periodicity of sampling and providing a rationale for these choices. If there is a gap between collection periods, state the dates for each sample cohort. Specify the spatial scale from which the data are taken*

Data exclusions *If no data were excluded from the analyses, state so OR if data were excluded, describe the exclusions and the rationale behind them, indicating whether exclusion criteria were pre-established.*

Reproducibility *Describe the measures taken to verify the reproducibility of experimental findings. For each experiment, note whether any attempts to repeat the experiment failed OR state that all attempts to repeat the experiment were successful.*

Randomization *Describe how samples/organisms/participants were allocated into groups. If allocation was not random, describe how covariates were controlled. If this is not relevant to your study, explain why.*

Blinding *Describe the extent of blinding used during data acquisition and analysis. If blinding was not possible, describe why OR explain why blinding was not relevant to your study.*

Did the study involve field work? Yes No

Reporting for specific materials, systems and methods

We require information from authors about some types of materials, experimental systems and methods used in many studies. Here, indicate whether each material, system or method listed is relevant to your study. If you are not sure if a list item applies to your research, read the appropriate section before selecting a response.

Materials & experimental systems

n/a	Involvement in the study
<input checked="" type="checkbox"/>	<input type="checkbox"/> Antibodies
<input checked="" type="checkbox"/>	<input type="checkbox"/> Eukaryotic cell lines
<input checked="" type="checkbox"/>	<input type="checkbox"/> Palaeontology and archaeology
<input checked="" type="checkbox"/>	<input type="checkbox"/> Animals and other organisms
<input checked="" type="checkbox"/>	<input type="checkbox"/> Human research participants
<input checked="" type="checkbox"/>	<input type="checkbox"/> Clinical data
<input checked="" type="checkbox"/>	<input type="checkbox"/> Dual use research of concern

Methods

n/a	Involvement in the study
<input checked="" type="checkbox"/>	<input type="checkbox"/> ChIP-seq
<input checked="" type="checkbox"/>	<input type="checkbox"/> Flow cytometry
<input checked="" type="checkbox"/>	<input type="checkbox"/> MRI-based neuroimaging